High Performance Frequency Converter Controlled Variable-Speed Wind Generator Using Linear-Quadratic Regulator Controller

Mahmoud A. Soliman[1], Hany M. Hasanien[2], *Senior Member, IEEE*, Ahmed Al-Durra[3], *Senior Member, IEEE* and Mahdi Debouza[3]

***Abstract*—This article proposes an optimal control strategy with a view to achieving the best performance of a wind energy conversion system (WECS). The optimal control strategy depends on the linear-quadratic regulator (LQR) algorithm, which provides fast convergence and less mathematical intricacy. The machine- and the grid-side converter/inverter are adjusted using the LQR controller. In this study, the system model and its control strategies are illustrated. Practical wind speed data are considered in this study for achieving realistic responses. The system performance is evaluated by comparing the results obtained using the LQR controller with that realized when the grey wolf optimizer algorithm-based optimized proportional-integral controllers are used, taken into account severe network disturbances. The simulation studies are extensively performed through the MATLAB/Simulink environment that prove the validity of the LQR controller for improving the performance of the WECS. The simulation results are compared with the experimental results for more validation.**

***Index Terms*—Frequency converter, linear-quadratic regulator (LQR), permanent-magnet synchronous generator, power system control, variable-speed wind turbine.**

I. INTRODUCTION

WIND power is considered the mainstream clean energy source in the electric power generation. Political matters, the depletion in fossil-fuel, and the rise in fuel prices are the main reasons that allow wind power to penetrate the power networks. In 2017, the cumulative global wind power capacity reached 539 GW, which is an increase of 11% compared with 2016 [1]. By 2022, it is predictable that the cumulative wind power capacity shall realize 840 GW worldwide [1].

The variable-speed wind turbine generator systems (WTGSs) are vastly applied in wind power applications because of the lower mechanical stress, the better control capability, and the high efficiency that they present than the fixed-speed [2], [3]. Different classes of electric machines are utilized in the variable-speed WTGSs. Among them, permanent-magnet synchronous generator (PMSG) has received great concerns in the modern wind industry because of the self-excitation and the high efficiency [4]–[6].

The variable-speed (VS)-WTGS driving PMSG is integrated into the grid via a full capacity frequency converter. The frequency converter consists of two power converters, which are tied through a dc-link [3], [6]. Each converter has six insulated gate bipolar transistors (IGBTs). However, this topology uses more controlled switches, resulting in the system is more expensive and less reliable. Few research efforts have been exerted to produce high-performance, simple, and reliable power converters with reduced number of power switches, losses, and cost in order to track the industrial requirements. The four-switch three-phase (FSTP) converter has been presented with four power switches as a substitute to the six-switch three-phase (SSTP) converter. The FSTP converter has some features over the SSTP converter, such as reduced the number of utilized switches by one-third, reduced the complexity of the driving circuits, where there are only two controlled branches which require only two interface driving circuits, and the maximum common mode voltage of the FSTP converter is two-thirds that of SSTP converter [7], [8].

Traditionally, the control of the machine-side converter (MSC) and the grid-side inverter (GSI) uses the proportional-integral (PI) controllers because of the robustness and the wide stability margins of these controllers [3]. However, these controllers have high sensitivity to the system nonlinearity and variables' uncertainty.

Several optimization approaches are presented for optimally designing the PI controllers [9]–[15]. Shuffled frog leaping algorithm [10], harmony search algorithm [11], grey wolf optimization [3], whale optimization algorithm [13], gravitational search algorithm [14], and water cycle algorithm [15] are proposed to design proper values of multiple PI controllers under the cascaded structure to enhance the behavior of grid-tied WECSs.

The grey wolf optimizer (GWO) algorithm is an evolutionary algorithm, which is used to optimally-tuning the PI controllers. The GWO is a new meta-heuristic optimization-based algorithm, which describes the grey wolves in wildlife [14].

Manuscript received June 27, 2019.

[1]Mahmoud A. Soliman is with the Dynamic Positioning Department, Petroleum Marine Services Company, Alexandria 22776, Egypt (e-mail: dr.msoliman08@gmail.com).

[2]Hany M. Hasanien is with the Electrical Power and Machines Department, Faculty of Engineering, Ain Shams University, Cairo 11517, Egypt (e-mail: hanyhasanien@ieee.org).

[3]Ahmed Al-Durra and Mahdi Debouza are the Advanced Power and Energy Center, EECS Department, Khalifa University, Abu Dhabi 2533, UAE (e-mail: ahmed.aldurra@ku.ac.ae, mahdi.debbouza@ku.ac.ae).

This article has been accepted for publication in a future issue of this journal, but has not been fully edited. Content may change prior to final publication. Citation information: DOI 10.1109/TIA.2020.2996956, IEEE Transactions on Industry Applications

The procedures of hunting behavior for the GWO algorithm are drawn by the grey wolves as; search, encircle, and attack the prey [16]–[18]. The GWO is characterized by the simple implementation, free-derivative technique, and lower operators to be adjusted compared to other optimization algorithms.

To overcome the complicated control strategies, Linear-Quadratic Regulator (LQR) is an alternative controller, presented to achieve the best dynamic performance and robust control stability. Generally, LQR is a state-feedback controller that utilizes a state-space approach to design and control the system. In LQR controller, the optimization relies on the minimization of quadratic cost function [19]. The main merits of LQR controller include superior performance without sophisticated algorithms and extra computational analysis. The LQR controller is simple, easy to implement, and has a lower memory capacity [20]. These advantages of the LQR represent the impetus to use it in this study to obtain better results than other traditional controllers. The LQR controller has been extensively applied to efficiently control many industrial applications such as aerospace engineering and technology [21], discrete-time control systems [22], hybrid systems [23], laser beam shaping [24], electric drives [25] and wind energy systems [26], [27].

This paper introduces the LQR controller-based an optimal control scheme for improving the characteristics of a grid-connected variable-speed WTGS. A low-cost frequency converter, which consists of two identical FSTP converters, is presented. To control the MSC and the GSI, a hysteresis current controller is considered. Moreover, a rotor position estimator based on a sliding mode observer (SMO) technique is established to reduce the cost and the hardware intricacy. The main new contribution of this study is the novel application of the LQR controller to control the FSTP converters of the VS-WTGS. The proposed controller validity is verified with both the simulation and experimental results under grid disturbance conditions. The model system and its control schemes are illustrated. Realistic wind speed data are considered in this study to achieve realistic responses. The system performance is evaluated by comparing the results obtained using the proposed LQR controller with that realized when the GWO algorithm-based optimized PI controllers are used, taken into account severe network fault conditions. The simulation analyses are performed through the MATLAB/Simulink environment that verifies the validity of the LQR controller.

II. Model of the Wind Turbine

The output power extracted from the wind is mathematically described as [28]-[30]:

$$P_\omega = 0.5\rho\pi R^2 V_\omega^3 C_P(\lambda,\beta) \quad (1)$$

where P_ω represents the output power from the wind [W], ρ denotes the density of air [kg/m3], R represents the radius of the turbine's blade [m], V_w is the wind speed [m/s], and C_P denotes the power coefficient, λ represents tip speed ratio, and β denotes blade pitch angle [deg.].

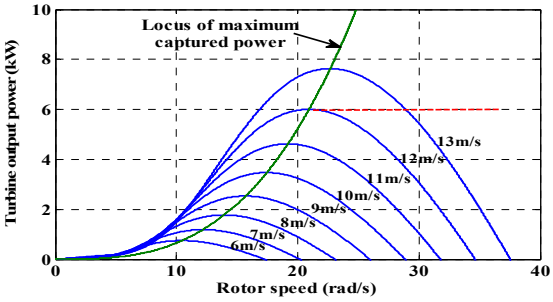

Fig. 1. Wind turbine characteristics with MPPT.

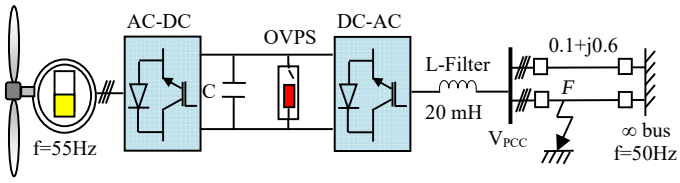

Fig. 2. Model system.

The C_P coefficient can be described as follows [3]:

$$C_P(\lambda,\beta) = 0.5(\lambda - 0.022\beta^2 - 5.6)e^{-0.17\lambda} \quad (2)$$

$$\lambda = \frac{\omega_r R}{V_w} \quad (3)$$

where ω_r denotes the blade rotor speed [rad/s].

Fig. 1 points out the characteristics of the wind turbine with the maximum power point tracking (MPPT). The maximum output power captured from the wind in terms of rotor speed is described by the following [6]:

$$P_{max} = 0.5\rho\pi R^2 \left(\frac{\omega_r R}{\lambda_{opt}}\right)^3 C_{P-opt} \quad (4)$$

where C_{P-opt} and λ_{opt} are the optimum values of the C_P and λ, respectively.

III. Model System

Fig. 2 shows the system modelling to explain the efficacy of the proposed LQR controller utilized for adjusting the frequency converter of the variable-speed wind turbine (VSWT) driving PMSG. The VSWT-PMSG system consists of a VSWT, a PMSG connected to the electric network via a full capacity frequency converter, and a double-circuit transmission line. In this study, the rated power and frequency of the PMSG is 6.0 kW and 55 Hz, respectively. More details of the PMSG data are reported in [28].

IV. Speed Estimator Based on SMO Technique

The information of the rotor position signal of the PMSG is necessary needed for the system control. In this study, the sliding-mode observer (SMO) technique is applied for sensorless rotor position estimation of the PMSG. The observer depends on the measured stator voltages and currents of the PMSG, where the $\alpha\beta$ coordinates of the actual voltages and currents are the inputs to the SMO. The $\alpha\beta$ stator current components are given as [31]:

$$\frac{di_\alpha}{dt} = -\frac{R_s}{L_s} i_\alpha + \frac{1}{L_s} v_\alpha - \frac{1}{L_s} e_\alpha \quad (5)$$

This article has been accepted for publication in a future issue of this journal, but has not been fully edited. Content may change prior to final publication. Citation information: DOI 10.1109/TIA.2020.2996956, IEEE Transactions on Industry Applications

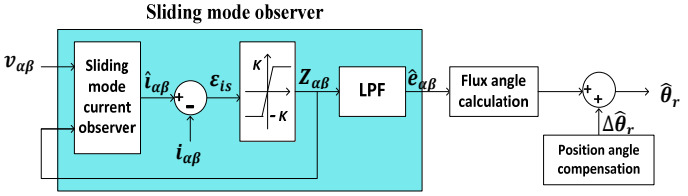

Fig. 3. Schematic diagram of the rotor position estimation using SMO.

$$\frac{di_\beta}{dt} = -\frac{R_s}{L_s} i_\beta + \frac{1}{L_s} v_\beta - \frac{1}{L_s} e_\beta \tag{6}$$

$$e_\alpha = -\omega_e \lambda_m sin\theta_r \tag{7}$$

$$e_\beta = \omega_e \lambda_m cos\theta_r \tag{8}$$

where R_s is stator resistance of the PMSG, L_s is the synchronous inductance of the PMSG, (v_α, v_β), (i_α, i_β), and (e_α, e_β) are the $\alpha\beta$ quantities of the stator voltages, currents, and back EMFs, respectively; and θ_r represents the rotor position. The estimated $\alpha\beta$ stator current components using SMO technique can be expressed as:

$$\frac{d\hat{\imath}_\alpha}{dt} = -\frac{R_s}{L_s} \hat{\imath}_\alpha + \frac{1}{L_s} v_\alpha - \frac{1}{L_s} \hat{e}_\alpha \tag{9}$$

$$\frac{d\hat{\imath}_\beta}{dt} = -\frac{R_s}{L_s} \hat{\imath}_\beta + \frac{1}{L_s} v_\beta - \frac{1}{L_s} \hat{e}_\beta \tag{10}$$

$$Z_{\alpha\beta} = k\ sgn\ \varepsilon_{is} = k\ sgn\ (\hat{\imath}_{\alpha\beta} - i_{\alpha\beta}) \tag{11}$$

where superscript ^ denotes the estimated quantities; $Z_{\alpha\beta}$ is the switching signal; sgn( ) represents the sign function, and k represents the switching gain of the observer.

To guarantee the convergence of the SMO, k should be selected such that $\varepsilon_{is} \cdot \left(\frac{d}{dt}\varepsilon_{is}^T\right) < 0$.

Fig. 3 clarifies the schematic diagram of the SMO. A low-pass filter is utilized to obtain the estimated back-EMF from the $Z_{\alpha\beta}$ as follows:

$$\hat{e}_\alpha = \frac{\omega_c}{S+\omega_c} Z_\alpha \tag{12}$$

$$\hat{e}_\beta = \frac{\omega_c}{S+\omega_c} Z_\beta \tag{13}$$

where ω_c represents the cut-off frequency of the filter.

The estimated rotor position can be obtained as:

$$\hat{\theta}_r = -tan^{-1}\left(\frac{\hat{e}_\alpha}{\hat{e}_\beta}\right) \tag{14}$$

As the filter causes phase delay, compensation is needed for the estimated angle, which is expressed as:

$$\Delta\hat{\theta}_r = tan^{-1}\left(\frac{\omega_e}{\omega_c}\right) \tag{15}$$

Hence, the estimated rotor speed can be obtained using the derivative of the estimated rotor angle.

V. Frequency Converter Modeling and Control Strategy

In this study, Fig. 4 presents the electrical configuration of the proposed VSWT-PMSG topology. The frequency converter of VSWT-PMSG illustrated in Fig. 4, consists of two identical FSTP power converters, one of them for the converter and the other for the inverter, and a two-split capacitor in the dc-link. A

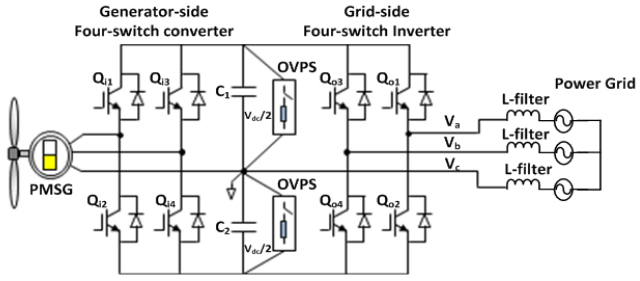

Fig. 4. Electrical configuration of VSWT-PMSG.

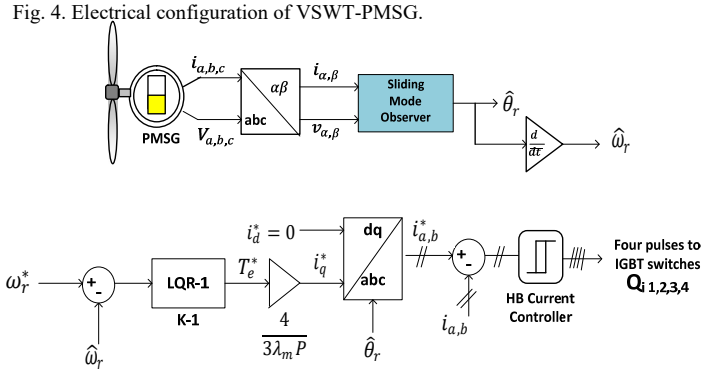

Fig. 5. Control blocks for the MSC.

FSTP inverter with the two-split capacitor achieves a balanced three-phase output to the power grid with adjustable voltage and frequency. The generator's terminals are directly tied to the two pulse width modulation voltages of the converter and the midpoint of the two-split capacitor. The three-phase power grid is tied to the two-leg inverter's output and the same midpoint. The midpoint of the split-capacitor acts as the third phase for the converter/inverter.

This control scheme is simple and achieves a good dynamic response [7]. The output phase voltages of the FSTP inverter as a function of switching states, S_a and S_b of the power switches and the voltage across the two-split capacitor, V_{dc}, are expressed in a matrix form as follows:

$$\begin{bmatrix} V_a \\ V_b \\ V_c \end{bmatrix} = \frac{V_{dc}}{3} \begin{bmatrix} 4 & -2 \\ -2 & 4 \\ -2 & -2 \end{bmatrix} \begin{bmatrix} S_a \\ S_b \end{bmatrix} + \frac{V_{dc}}{3} \begin{bmatrix} -1 \\ -1 \\ 2 \end{bmatrix} \tag{16}$$

A. The MSC

The MSC takes responsibility for capturing the maximum output power from the wind turbine and transmitting it to the grid. To achieve this target, a hysteresis current controller is used where the estimated generator speed ($\hat{\omega}_r$) is forced to track the reference speed (ω_r^*). The error signal between the reference and measured speeds generates the torque command (T_e^*) through the LQR controller. The q-axis current (i_q^*) is calculated from the T_e^* to control the active power. The i_d^* is chosen zero to ensure a maximum torque per minimum current. As a result, the resistive losses in the PMSG can be minimized. The dq-axes current quantities are converted to the three-phase reference currents using the estimated rotor angle ($\hat{\theta}_r$). The sensed two-phase currents ($i_{a,b}$) of the PMSG are then

This article has been accepted for publication in a future issue of this journal, but has not been fully edited. Content may change prior to final publication. Citation information: DOI 10.1109/TIA.2020.2996956, IEEE Transactions on Industry Applications

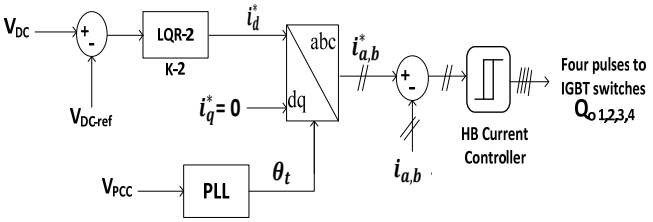

Fig. 6. Control blocks for the GSI.

compared with the two-phase reference currents ($i^*_{a,b}$) using two hysteresis comparators. The output signals of these comparators produce the switching pulses to the four electronic switches. The block diagram for the MSC is shown in Fig. 5.

B. The GSI

The main purpose of using the GSI is to adjust the dc-link voltage (V_{DC}) and keep it constant at the desired value and perform a unity power factor operation at the grid. In this study, two dc-link capacitors with rated values of 500 μF are considered and the V_{DC} is chosen 700 V for each one. The operation of the GSI is performed using the hysteresis current controller, where the V_{DC} is forced to track the dc-link reference voltage (V_{DC-ref}). The error signal between the reference and actual dc-link voltages produces the d-axis current (i^*_d) using the LQR controller. The i^*_q can control the reactive power. So, it is set zero to provide unity power factor operation at the grid terminals. The dq-axes currents are transformed to the abc components using the transformation angle (θ_t) achieved from the phase locked loop (PLL) system that employs the voltages at the point of common coupling (V_{PCC}). The actual two-phase currents at the grid-side ($i_{a,b}$) are compared with the two-phase current commands ($i^*_{a,b}$) using two independent hysteresis comparators that produce the firing pulses to the two-leg inverter. The block diagram of the GSI control is illustrated in Fig. 6 [32]-[34].

VI. The Proposed Controllers

A. LQR controller

The LQR is an optimal controller that employs a state-space system form to enhance the system response by using the suitable choice of state-feedback gain matrix (K). A pole placement method which depends on the desired location of poles is used to determine the values of K. Although the values of matrix (K) are easy to be calculated using this method, the LQR is a good choice for higher order and multi-input system where the best response of the closed-loop system is reached.

LQR depends on the cost function in order to define the optimal pole location. It uses differential equations that illustrate the paths of the control variables to decrease the cost function. The control input (u_c) is used to realize the optimal solution in which the quadratic cost function (J) can be minimized [19].

$$J = \int_0^\infty (x_e^T Q x_e + u_c^T R u_c)\, dt \tag{17}$$

where Q and R denote the weighted-matrices, which are selected to make the poles at the required location. When the matrix Q has large values, the closed-loop poles ($E = A - BK$) are becoming further left in the s-plane. As a result, the error decreases rapidly to zero. The matrix K is determined by the suitable selection of the weighted-matrices, where Q and R are positive semi-definite and positive definite, respectively.

The control input selected to decrease the quadratic cost function J is achieved as:

$$\mathrm{u_c} = -K x_e \tag{18}$$

where $x_e = x_{ref} - x_{actual}$.

The design of the optimal control scheme is realized by solving the Algebraic Riccati Equation:

$$A^T P + PA - PBR^{-1}B^T P + Q = 0 \tag{19}$$

Thus, the optimal K is obtained as:

$$K = R^{-1}B^T P \tag{20}$$

In this investigation, the control system is linearized in the state-space form as follows:

$$\dot{\mathrm{X}} = AX + BU \tag{21}$$

$$Y = CX \tag{22}$$

where X refers to the state variables, U represents the control input, and Y represents the control output.

For the PMSG model, the X, U, and Y can be expressed as follows:

$$X = [\, i_{d-PMSG} \;\; i_{q-PMSG} \;\; \omega_e]^T \tag{23}$$

$$U = [v_{ds-PMSG} \; v_{qs-PMSG} \;\; \lambda_m]^T \tag{24}$$

$$Y = [i_{d-PMSG} \;\; i_{q-PMSG} \;\; \omega_e]^T \tag{25}$$

For the power grid model, the X, U, and Y are written as follows:

$$X = [i_{d-Grid} \;\; i_{q-Grid}]^T \tag{26}$$

$$U = [v_{ds-Grid} \; v_{qs-Grid}]^T \tag{27}$$

$$Y = [i_{d-Grid} \;\; i_{q-Grid}]^T \tag{28}$$

where $v_{ds-Grid}$ and $v_{qs-Grid}$ denote dq-axes network voltages.

In this investigation, the error signal between the set-point and actual signals denote the performance index J. The error signal is the input to the LQR controller. In an instant, for LQR-1 presented in Fig. 5, the reference and measured signals are ω^*_r and $\hat{\omega}_r$, respectively, and the output of LQR controller represents the torque command (T^*_e).

The optimal values of Q and R used in this investigation are chosen to reach the optimal performance along with an economical cost as follows:

$Q = [Q\text{-}1 \;\; Q\text{-}2] = [1.18 \;\; 10]$; $R = [R\text{-}1 \;\; R\text{-}2] = [0.7 \;\; 2]$.

In this study, the MATLAB command "[K] = LQR (A, B, Q, R)" is used to obtain the optimal gain K, where the values of A and B are determined from the linearized system. The values of K for the system under study are determined as follows:

$K = [K\text{-}1 \;\; K\text{-}2] = [1.2984 \;\; 2.2361]$.

B. Optimized PI controller by GWO algorithm

GWO is a novel population-based approach presented in 2014

This article has been accepted for publication in a future issue of this journal, but has not been fully edited. Content may change prior to final publication. Citation information: DOI 10.1109/TIA.2020.2996956, IEEE Transactions on Industry Applications

[14]. The GWO algorithm describes the hunting behavior of the grey wolves. Grey wolves used to live in groups. The size of each group usually consists of 5-12 wolves. This group, in general, classified into four prevalent dominant types, named alpha (α), beta (β), delta (δ), and omega (ω) wolves. The α wolves represent the leader wolves in the group. They are responsible for taking social and activity works such as hunt, sleep place, and time to wake. Besides, the α wolves pursue other wolves in the group for some kind of democracy. The β wolves are the next level in the pack, who help and support α wolves in decisions-making. The β wolf is the best candidate to α wolf when α wolf dies or becomes too old. The β wolves are responsible for helping the α wolves and reinforce their order in the group. The final level of dominance in the group is the ω wolves, which are the last wolves that are allowed to eat. Sometimes, the ω wolves are the babysitters in the group. The δ wolves take the responsibility for presenting sufficient knowledge to α and β wolves; however they dominate ω wolves. The steps of hunting process of the grey wolves are broadly categorized as [16]–[18]:

1. Tracking, chasing, and approaching the prey.
2. Encircle and harass the prey until it stops moving.
3. Attack to the prey.

In this study, the GWO algorithm is used to design the values of the PI controllers, as mentioned in [3].

VII. Results And Discussion

The simulation studies are executed through the MATLAB/Simulink environment. The time step is considered 20 µs. The efficiency of the LQR controller is examined by comparing the analyses with that realized when the GWO-based optimal PI controllers is used, considering the normal and transient operating conditions, which are discussed as follows.

A. Normal Operating Condition

The dynamic response of the VSWT driven PMSG is verified through practical wind speed data captured from Zaafarana wind farm, Egypt, as pointed out in Fig. 7(a). The simulation time is 500 s, which indicates a wide speed range of the wind speed from 8.1 to 11.8 m/s that considered in this study. Fig. 7(b) shows the responses of the measured and estimated generator speeds. It can be noted here that the measured PMSG speed can track the estimated speed very well. Fig. 7(c) points out the responses of the measured and estimated rotor positions of the PMSG. Notably, the SMO technique can accurately estimate the rotor position/speed of the PMSG during all operating conditions. The optimum and grid active powers are shown in Fig. 7(d). Note that those powers are very close due to the power losses of converters. Fig. 7(e) indicates the reactive power at the GSI using the LQR controller. The terminal grid voltage at the PCC is shown in Fig. 7(f). The terminal grid current at the PCC is illustrated in Fig. 7(g). Notably, the FSTP frequency converter works very well with the VSWT-PMSG system. Moreover, the LQR controller can precisely capture the maximum power from the wind and deliver it to the utility grid during different operating conditions.

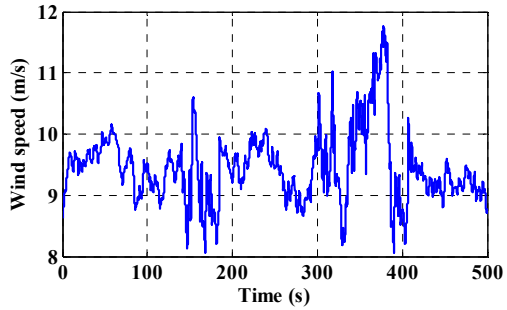

(a)

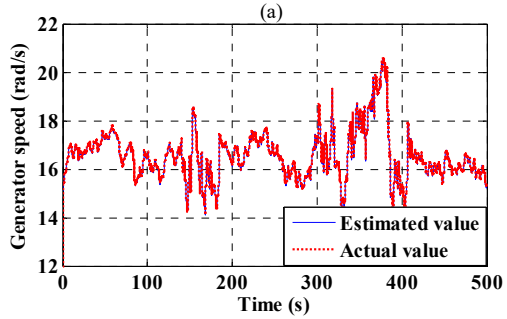

(b)

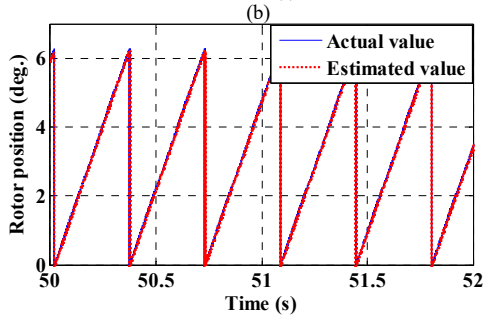

(c)

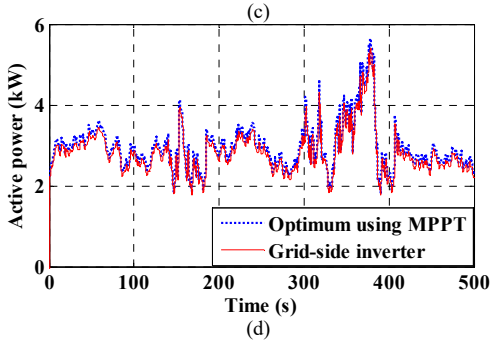

(d)

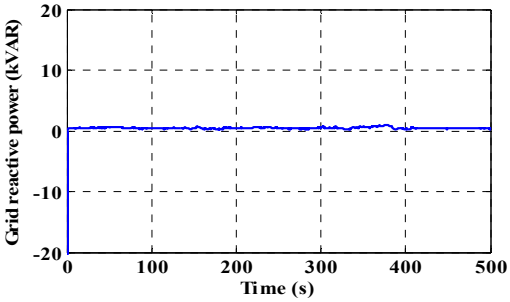

(e)

This article has been accepted for publication in a future issue of this journal, but has not been fully edited. Content may change prior to final publication. Citation information: DOI 10.1109/TIA.2020.2996956, IEEE Transactions on Industry Applications

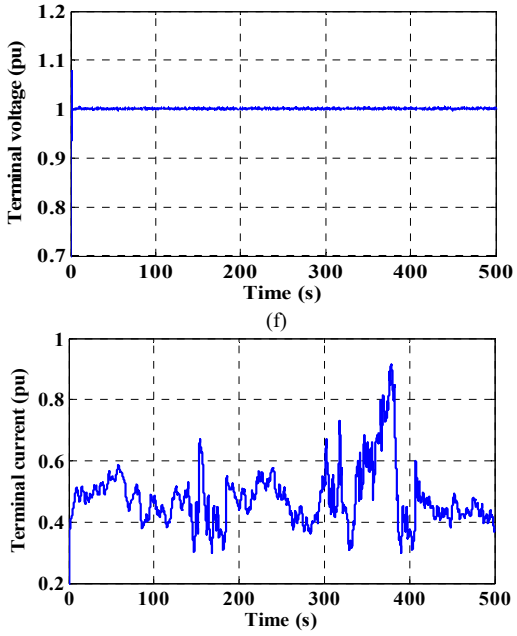

Fig. 7. Performances of LQR controllers with the help of using practical wind speed data (a) Wind speed. (b) Generator speed. (c) Rotor position of the PMSG. (d) Active power of the grid-side inverter. (e) Reactive power of the grid-side inverter. (f) Terminal grid voltage. (g) Terminal grid current.

B. Transient Fault Operating Condition

The validity of the LQR controller adjusted the power converters of the VSWT-PMSG integrated to the network is verified by subjecting the system to severe grid disturbance. The three-line-to-ground (3LG) fault happens at 1.5 s at the fault point *F*, as pointed out in Fig. 1. The circuit breakers (CBs) of this transmission line are opened together at 1.6 s for clearing the fault. At 1.7 s, the fault is cleared, and the CBs are reclosed together at 2.5 s. The wind speed remains constant at 12 m/s. During fault condition, an overvoltage protection scheme (OVPS), which is presented in [28], is employed in this investigation. The responses of the V_{dc} with/without using OVPS using both approaches are pointed out in Fig. 8(a). It is illustrated that the V_{dc} increases quickly at the moment of the fault. Therefore, the OVPS is considered to keep the V_{dc} within an admissible limit. The chopper current response is pointed out in Fig. 8(b). Fig. 8(c) demonstrates the response of the terminal grid voltage at the PCC using the LQR controller, which is improved compared to the GWO algorithm-based optimized PI controller. The reactive power responses of the GSI using both approaches are indicated in Fig. 8(d). Notably, the reactive power response at the GSI is more improved using the LQR control strategy than that reached when the optimal PI control strategy is employed.

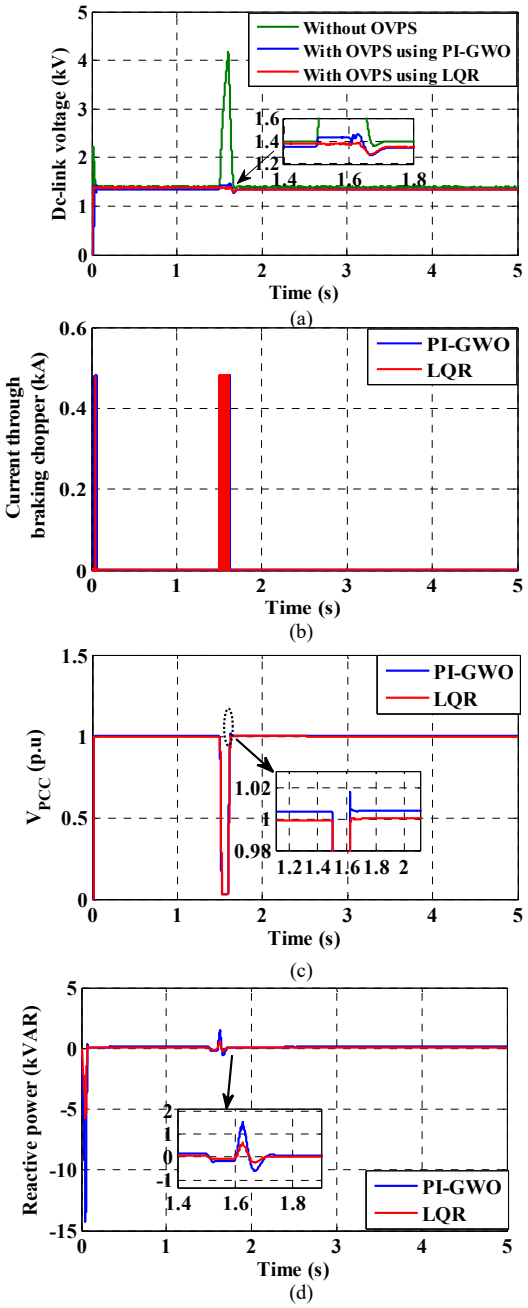

Fig. 8. Performances for 3LG fault (a) DC-link voltage. (b) Current through chopper. (c) Terminal grid voltage at the PCC. (d) Reactive power of the grid-side inverter.

VIII. Experimental Results

The proposed LQR LVRT improvement strategy is validated on a small-scale laboratory experimental setup. The setup consists of two coupled permanent magnet synchronous machines. The first machine acts like a motor to mimic the effect of a wind turbine, and the second acts as a power generator. The PMSM speed is controlled via 2-level IGBT based industrial 7 HP Danfoss FC 302 drive. The PMSM drive is supplied from an independent autotransformer. The PMSG is controlled using the same drive but with modified hardware configuration which allows direct access to the IGBT gates for external controllers implementations. Similarly, a third drive is used to control the gates of the GSC. The GSC and MSC power supplies and the grid voltage fault conditions are obtained using Cinergia GE-15 grid emulator [35]. The OVP is implemented using the drive brake feature where a chopper circuit with a high power ratings resistor is connected in parallel to the dc-link capacitor. The system currents and voltages measurements are obtained from the measurements sensors

This article has been accepted for publication in a future issue of this journal, but has not been fully edited. Content may change prior to final publication. Citation information: DOI 10.1109/TIA.2020.2996956, IEEE Transactions on Industry Applications

blocks. The PMSG torque is read from a torque meter mounted on the coupling point, and the angular position is monitored using a 1024 pulse per rotation rotary incremental encoder mounted on the PMSM shaft. The control strategies are implemented on a dspace 1202 MicrolabBox DSP board. The PMSG experimental setup is shown in Fig. 9(a), and the parameters of the setup are summarized in Table I. The LQR controller is implemented in the experimental setup. The system results using the LQR controller are compared with that achieved using the GWO-based PI controller, whose gains are listed in Table II.

The fault duration is achieved using the grid emulator by reducing the nominal grid voltage for a desired duration. Fig. 9(b) shows the system Vdc response to a 10% voltage magnitude drop and 100 ms fault duration. This figure shows the system dc-link voltages response during the fault. A vertical offset of 324 V is added to show the dynamic response. The dc-link voltage reference Vdc* is set to 350V. It can be clearly seen from Fig. 9(b) that the voltage is precisely controlled to the reference value. When the fault occurs at t=0.8 s, Vdc decreases and then increases. The decrease is due to the fault where power is observed by the OVP. On the other hand, the increase occurs as the fault is cleared and Vdc is controlled back to the reference value. It can be noted form the Vdc response that the control approach has a significant impact on the system behavior. The LQR controller has less impact on the Vdc decrease, lower overshoot, and faster recovery after the fault compared with the GWO controller.

Fig. 9(c) demonstrates Vpcc response during the fault. A vertical offset of 105 V is added to show the dynamic response of Vpcc. The reference rms voltage Vpcc* is set to 117 rms. The rms voltage drops during the fault. Vpcc returns back to Vpcc* after the fault. Similarly, the controller gains provided by the LQR controller have enhanced transient and steady-state performances. Fig. 9(d) indicates the active powers response during the fault. In the channel plots, the voltage to active power ratio is unity. The fault duration is very small; thus, the wind speed is assumed to be constant during the fault. Therefore, the PMSG torque reference is set to 100 N.m with a constant speed of 150 rpm in this test. The grid active power declines during the fault and then returns to nominal value. The LQR controller response is faster and smoother than the GWO response. The OVP chopper resistor is enabled only during the fault, and this can be seen from the chopper resistor current. Fig. 9(e) shows the reactive power response during the fault. In the channel plots, the voltage to reactive power ratio is unity. The reactive power support increases during the fault to help in supporting Vpcc. It can be noted from Fig. 9(e) that the grid reactive power supplied by LQR controller is higher than the one supplied by the GWO controller, and this explains the enhanced effect on voltage responses.

Fig. 9(a). PMSG Experimental setup.

TABLE I
PMSG EXPERIMENTAL SETUP PARAMETERS.

Parameters	Values
Nominal voltage	117 V rms (ph-to-n)
System frequency	50 Hz
Dc-link voltage	350 V
Dc-link capacitance	350 µF
Filter inductance	3.3 mH
Grid inductance	0.8 mH
PMSG rated power	5 kW
Number of poles	22
PMSG rated speed	240 rpm
PMSG winding resistance	0.84 Ω
PMSG winding d-axis inductance	12.6 mH
PMSG winding q-axis inductance	21.8 mH

TABLE II
CONTROLLER GAINS USING GWO

Controllers Gains	Notation	GWO
Vdc outer-loop proportional gain	Kp_{Vdc}	0.07
Vdc outer-loop integral gain	Ki_{Vdc}	1.2
Vpcc outer-loop proportional gain	Kp_{Vpcc}	0.3
Vpcc outer-loop integral gain	Ki_{Vpcc}	1.5
Inner - loop proportional gain	Kp_{GSC}	5
Inner - loop integral gain	Ki_{GSC}	26

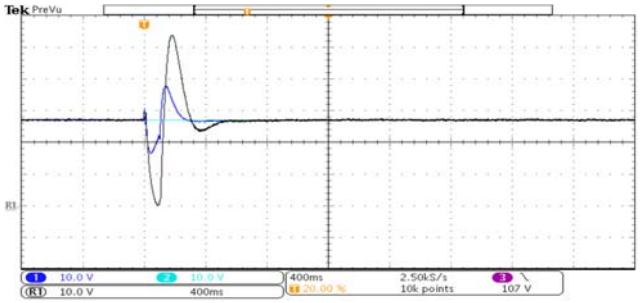

Fig. 9(b). Vdc response to fault (Ch-1 Vdc LQR, Ch-2 Vdc*, R1 Vdc GWO).

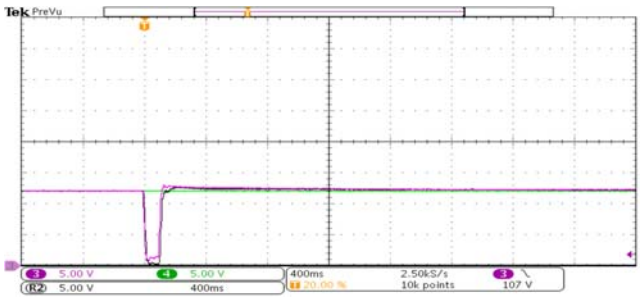

Fig. 9(c). Vpcc response to fault (Ch-3 Vpcc LQR, Ch-4 Vpcc*, R2 Vpcc GWO).

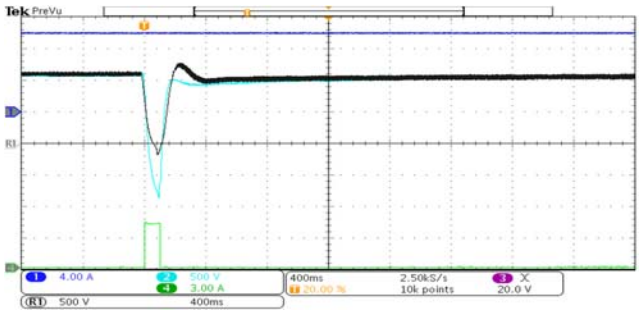

Fig. 9(d). Active power response to fault (Ch-1 IqPMSG, Ch-2 PGSC LQR, R1 PGSC GWO, Ch-4 Current through the chopper resistor).

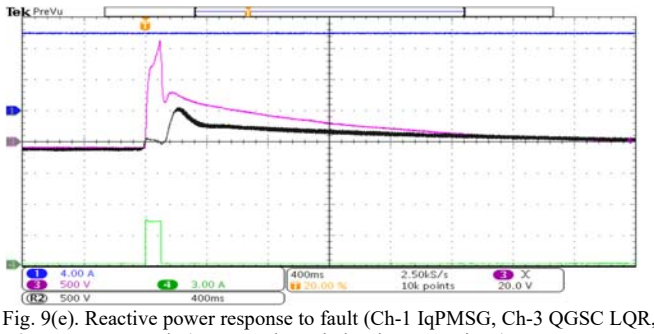

Fig. 9(e). Reactive power response to fault (Ch-1 IqPMSG, Ch-3 QGSC LQR, R2 QGSC GWO, Ch-4 Current through the chopper resistor).

IX. Conclusion

This article has proposed an LQR control scheme to optimally control the FSTP frequency converter with a view to improve the characteristics of the WECS. The proposed control scheme was introduced to control the MSC and the GSI. The rotor position and speed of the PMSG have been estimated using the SMO algorithm. Therefore, eliminating the rotor position/speed sensors with reducing the number of utilizing power switches will be advantageous in terms of cost/losses, and reliability. The simulation and experimental results have proven the validation of the LQR controller in obtaining the best responses by comparing the results to that realized when the GWO algorithm-based optimized PI control strategy is employed. The transient specifications like maximum percentage overshoot, undershoot, rise time, settling time, and steady state error of several quantities are smaller using the LQR controller and these specifications with the LQR controller are lower than that achieved by the PI controller by at least 20%. Moreover, the LQR controller is very simple, easy to implement, and has a lower memory capacity. The results have also shown its verification of smooth dynamic operation under real wind speed data extracted from a wind power plant. It can be concluded that the LQR is an optimal control approach that has the capability to deal well with the system uncertainty and enhancing system stability.

References

[1] Global Wind Energy Council (GWEC), "Annual market update 2015," Global Wind Report, available at: http://www.gwec.net

[2] X. Zeng, J. Yao, Z. Chen, W. Hu, Z. Chen, and T. Zhou, "Co-ordinated control strategy for hybrid wind farms with PMSG and FSIG under unbalanced grid voltage condition," *IEEE Trans. Sustain. Energy*, vol. 7, no. 3, pp. 1100–1110, 2016.

[3] Mahmoud A. Soliman, Hany M. Hasanien, Haitham Z. Azazi, et al., "Hybrid ANFIS-GA-based control scheme for performance enhancement of a grid-connected wind generator," *IET Renew. Power Gener*., vol. 12, no. 7, pp. 832–843, 2018.

[4] Z. Zhang, F. Wang, J. Wang, J. Rodríguez, and R. Kennel, "Nonlinear direct control for three-level NPC back-to-back converter PMSG wind turbine systems: experimental assessment with FPGA," *IEEE Trans. Ind. Inf*., vol. 13, no. 3, pp. 1172–1183, 2017.

[5] J. Chen, T. Lin, C. Wen, and Y. Song, "Design of a unified power controller for variable-speed fixed-pitch wind energy conversion system," *IEEE Trans. Ind. Electron.*, vol. 63, no. 8, pp. 4899–4908, 2016.

[6] Mahmoud A. Soliman, Hany M. Hasanien, Haitham Z. Azazi, et al., "An adaptive fuzzy logic control strategy for performance enhancement of a grid-connected PMSG-based wind turbine," *IEEE Trans. Ind. Inf*., vol. 15, no. 6, pp. 3163-3173, June 2019.

[7] M. K. Metwally and H. Z. Azazi, "Four-switch three-phase inverter performance fed sensorless speed control induction motor drives using model reference adaptive system," *Elect. Power Compon. Syst*., vol. 42, no. 7, pp. 727–736, 2014.

[8] D. Zhou, J. Zhao, and Y. Liu, "Predictive torque control scheme for three-phase four-switch inverter-fed induction motor drives with DC-link voltages offset suppression," *IEEE Trans. Power Electron*., vol. 30, no. 6, pp. 3309–3318, 2015.

[9] Hany M. Hasanien and S. M. Muyeen, "Particle swarm optimization-based superconducting magnetic energy storage for low-voltage ride-through capability enhancement in wind energy conversion system," *Elect. Power Compon. Syst*., vol. 43, no. 11, pp. 1278–1288, 2015.

[10] Hany M. Hasanien, "Shuffled frog leaping algorithm-based static synchronous compensator for transient stability improvement of a grid-connected wind farm," *IET Renew. Power Gener.*, vol. 8, no. 6, pp. 722–730, 2014.

[11] M. N. Ambia, H. M. Hasanien, A. Al-Durra, and S. M. Muyeen, "Harmony search algorithm-based controller parameters optimization for a distributed-generation system," *IEEE Trans. Power Del*., vol. 30, no. 1, pp. 246–255, Feb. 2015.

[12] Hany M. Hasanien, "Design optimization of PID controller in automatic voltage regulator system using Taguchi combined genetic algorithm method," *IEEE Syst. J*., vol. 7, no. 4, pp. 825–831, 2013.

[13] Hany M. Hasanien, "Performance improvement of photovoltaic power systems using an optimal control strategy based on whale optimization algorithm," *Electric Power Syst. Research*., vol. 157, pp. 168–176, 2018.

[14] Hany M. Hasanien, "Gravitational search algorithm-based optimal control of archimedes wave swing-based wave energy conversion system supplying a DC microgrid under uncertain dynamics," *IET Renew. Power Gener*., vol. 11, no. 6, pp. 763–770, 2017.

[15] Hany M. Hasanien and M. Matar, "Water cycle algorithm-based optimal control strategy for efficient operation of an autonomous microgrid', *IET Gener. Transm. Distrib*., vol. 12, no. 21, pp. 5739–5746, 2018.

[16] S. Mirjalili, S. M. Mirjalili, and A. Lewis, "Grey wolf optimizer," *Adv. Eng. Soft.*, vol. 69, no. 3, pp. 46–61, 2014.

[17] C. Muro, R. Escobedo, L. Spector, and R. Coppinger, "Wolf-pack (Canis lupus) hunting strategies emerge from simple rules in computational simulations," *Behav. Process*., vol. 88, no. 3, pp. 192–197, 2011.

[18] Attia A. El-Fergany and Hany M. Hasanien, "Single and multi-objective optimal power flow using grey wolf optimizer and differential evolution algorithms," *Elect. Power Compon. Syst*., vol. 43, no. 13, pp. 1548–1559, 2015.

[19] C. Olalla, R. Leyva, A. El Aroudi, and I. Queinnec, "Robust LQR control for PWM converters: an LMI approach," *IEEE Trans. Ind. Electron*., vol. 56, no.7, pp. 2548–2558, 2009.

[20] K. Ogata, "Modern control engineering," PHI Learning Private Limited, 2011.

[21] M. J. Mahmoodabadi and N. R. Babak, "Robust fuzzy linear quadratic regulator control optimized by multi-objective high exploration particle swarm optimization for a 4 degree-of-freedom quadrotor," *Aerospace Sc. Tech*., vol. 97, 105598, pp. 1–13, Feb. 2020.

[22] H. Zhang, J. Umenberger and X. Hu, "Inverse optimal control for discrete-time finite-horizon linear quadratic regulators," *Automatica*, vol. 110, 108593, pp. 1–9, December 2019.

[23] C. Possieri, M. Sassano, S. Galeani, and A. R. Teel, "The linear quadratic regulator for periodic hybrid systems," *Automatica*, vol. 113, 108772, pp. 1–12, March 2020.

[24] J. C. Aguero, S. Zuniga, M. Castro, and J. Garces, "Linear quadratic regulator for laser beam shaping," *Optics Lasers Eng.*, vol. 94, pp. 90–96, July 2017.
[25] T. Shi, Y. Yan, Z. Zhou, M. Xiao, and C. Xia, "Linear quadratic regulator control for PMSM drive systems using nonlinear disturbance observer," *IEEE Trans. Power Elec.*, vol. 35, no. 5, pp. 5093–5101, May 2020.
[26] D. Kumar and K. Chatterjee, "Analysis and enhancement of small-signal stability of DFIG-based wind integrated power system through the optimal design of linear quadratic regulator," *IET Renew. Power Gener*., vol. 14, no. 4, pp. 628–639, 2020.
[27] S. Nallusamy, D. Velayutham, and U. Govindarajan, "Design and implementation of a linear quadratic regulator controlled active power conditioner for effective source utilisation and voltage regulation in low-power wind energy conversion systems," *IET Power Electron*., vol. 8, no. 11, pp. 2145–2155, 2015.
[28] Mohammed H. Qais, Hany M. Hasanien and Saad Alghuwainem, "Enhanced whale optimization algorithm for maximum power point tracking of variable- speed wind generators", *App. Soft Comp.,* vol. 86, 105937, pp. 1-14, January 2020.
[29] Mohammed H. Qais, Hany M. Hasanien and Saad Alghuwainem, "Output power smoothing of wind power plants using self-tuned controlled SMES units ", *Elec. Power Sys. Res.,* vol. 178, 106056, pp. 1-9, January 2020.
[30] Farzana Islam, Hany M. Hasanien, Ahmed Al-Durra, and S.M.Muyeen, "A New Control Strategy for Smoothing of Wind Farm Output using Short-Term Ahead Wind Speed Prediction and Flywheel Energy Storage System", *Proc. American Con. Con., ACC*, 27-29June 2012, Montreal, Canada.
[31] Z. Zhang, Y. Zhao, W. Qiao, and L. Qu, " A space-vector-modulated sensorless direct-torque control for direct-drive PMSG wind turbines," *IEEE Trans. Ind. Appl*., vol. 50, no. 4, pp. 2331–2341, 2015.
[32] Mohammed H. Qais, Hany M. Hasanien, and Saad Alghuwainem, "Enhanced salp swarm algorithm: Application to variable speed wind generators", *Eng. Appl. Artific. Intel.,* vol. 80, pp. 82-96, April 2019.
[33] Mohammed H. Qais, Hany M. Hasanien, and Saad Alghuwainem, "A Grey wolf optimizer for optimum parameters of multiple PI controllers of a grid-connected PMSG driven by variable speed wind turbine", *IEEE Access,* vol. 6, no. 1, pp. 44120-44128, December 2018.
[34] Mahmoud A. Soliman, Hany M. Hasanien and Ahmed Al-Durra, "High performance frequency converter controlled variable-speed wind generator using linear-quadratic regulator controller", *The IEEE Ind. App. Soc. Ann. Meeting,* pp. 1-7, 29 September-3 October 2019, Baltimore, MD, USA.
[35] Omnia S. Elazab, Mahdi Debouza, Hany M. Hasanien, S. M. Muyeen, and Ahmed Al-Durra, "Salp swarm algorithm-based optimal control scheme for LVRT capability improvement of grid-connected photovoltaic power plants: design and experimental validation", *IET Renew. Power Gener.,* vol. 14, no. 4, pp. 591-599, March 2020.

Mahmoud A. Soliman He received the B.Sc., M.Sc., and Ph.D. degrees in electrical engineering from Faculty of Engineering, Menoufia University, Shebin El-Kom, Egypt, in 2008, 2013, 2019, respectively.

He joined Oil and Gas industry as an Electrical Engineer in 2009 up till now. Since 2013, he has been engaged in scientific research of power electronics and renewable power systems. His research interests include electrical drives, modern control techniques, renewable energy systems, micro- and smart grids, and artificial intelligence applications on electrical machines and renewable energy systems. Dr. Soliman is a Reviewer in different international journals like the IET and Elsevier.

Hany M. Hasanien (SM 11) received his B.Sc., M.Sc. and Ph.D. degrees in Electrical Engineering from Ain Shams University, Faculty of Engineering, Cairo, Egypt, in 1999, 2004, and 2007, respectively. From 2008 to 2011, he was a Joint Researcher with Kitami Institute of Technology, Kitami, Japan. Currently, he is Professor at the Electrical Power and Machines Department, Faculty of Engineering, Ain Shams University. His research interests include modern control techniques, power systems dynamics and control, energy storage systems, renewable energy systems, and smart grid. He has authored, co-authored, and edited three books in the field of electric machines and renewable energy. He has published more than 120 papers in international journals and conferences. Prof. Hasanien is an Editorial Board Member of *Electric Power Components and Systems Journal*. He is Subject Editor of IET Renewable Power Generation.

Ahmed Al-Durra received his PhD in ECE from Ohio State University in 2010. He is an Associate Professor in the ECE Department at Khalifa University, UAE. His research interests are applications of control and estimation theory on power systems stability, micro and smart grids, renewable energy systems and integration, and process control. He has one US patent, one edited book, 12 book chapters, and over 190 scientific articles in top-tier journals and refereed international conference proceedings. He has supervised/co-supervised over 25 PhD/Master students. He is leading the Energy Systems, Control & Optimization Lab at ADNOC Research & Innovation Center, an Editor for IEEE Transactions on Sustainable Energy and IEEE Power Engineering Letters, and Associate Editor for IEEE Transactions on Industry Applications and Frontiers in Energy Research – Smart Grids.

MAHDI DEBOUZA (SM'11–M'18) received the B.Sc. degree from Abu Dhabi University, Abu Dhabi, United Arab Emirates, in 2014 and the M.Sc. degree from the Petroleum Institute, Khalifa University, Abu Dhabi, United Arab Emirates, in 2016, both in electrical engineering. He is currently a Research Assistant with Khalifa University. His research interests include renewable energy control and integration, electric machines and drives, energy management and storage, and smart grid technologies.